Journal of Energy Chemistry 50 (2020) 178–186

Contents lists available at ScienceDirect

Journal of Energy Chemistry

journal homepage: www.elsevier.com/locate/jechem

http://www.journals.elsevier.com/journal-of-energy-chemistry/

Visualizing the importance of oxide-metal phase transitions in the production of synthesis gas over Ni catalysts ☆

Luis Sandoval-Diaz [a], Milivoj Plodinec [a], Danail Ivanov [a], Stéphane Poitel [b], Adnan Hammud [a], Hannah C. Nerl [a], Robert Schlögl [a,c], Thomas Lunkenbein [a,*]

[a] Department of Inorganic Chemistry, Fritz-Haber-Institut der Max-Planck-Gesellschaft, Faradayweg 4-6, 14195 Berlin, Germany
[b] Electron Spectrometry and Microscopy Laboratory, School of Basic Sciences, École Polytechnique Fédérale de Lausanne, 1015 Lausanne, Switzerland
[c] Max Planck Institute for Chemical Energy Conversion, Stiftstraße 34-36, 45470 Mühlheim a.d. Ruhr, Germany

ARTICLE INFO

Article history:
Received 20 December 2019
Revised 28 February 2020
Accepted 4 March 2020
Available online 13 March 2020

Keywords:
Dry reforming of methane
Partial oxidation of methane
Environmental scanning electron microscopy
Synthesis gas
Operando

ABSTRACT

Synthesis gas, composed of H_2 and CO, is an important fuel which serves as feedstock for industrially relevant processes, such as methanol or ammonia synthesis. The efficiency of these reactions depends on the H_2: CO ratio, which can be controlled by a careful choice of reactants and catalyst surface chemistry. Here, using a combination of environmental scanning electron microscopy (ESEM) and online mass spectrometry, direct visualization of the surface chemistry of a Ni catalyst during the production of synthesis gas was achieved for the first time. The insertion of a homebuilt quartz tube reactor in the modified ESEM chamber was key to success of the setup. The nature of chemical dynamics was revealed in the form of reversible oxide-metal phase transitions and surface transformations which occurred on the performing catalyst. The oxide-metal phase transitions were found to control the production of synthesis gas in the temperature regime between 700 and 900 °C in an atmosphere relevant for dry reforming of methane (DRM, CO_2: CH_4 =0.75). This was confirmed using high resolution transmission electron microscopy imaging, electron energy loss spectroscopy, thermal analysis, and $C^{18}O_2$ labelled experiments. Our dedicated *operando* approach of simultaneously studying the surface processes of a catalyst and its activity allowed to uncover how phase transitions can steer catalytic reactions.

1. Introduction

The production of synthesis gas (CO and H_2 mixtures) was proposed by Fischer and Tropsch in 1928 [1]. Since then, synthesis gas has become an important feedstock for methanol [2–4] and ammonia synthesis [5]. Synthesis gas can be produced from the reactions of methane with water (Eq. (1)), oxygen (Eq. (2)) and carbon dioxide (Eq. (3)). The latter reaction, called dry reforming of methane (DRM), has obtained significant attention since it converts two greenhouse gases into valuable chemicals [6–10].

DRM is generally performed at temperatures above 650 °C in the presence of supported metallic catalysts. Precious metals such as Pt, Pd, Ru, and Rh are active reforming catalysts [10–12]. This process is usually accompanied by a cascade of side reactions:

$H_2O + CH_4 \rightarrow CO + 3H_2$ ΔH_{298}= 206 kJ mol^{-1} Steam reforming (1)

$½\ O_2 + CH_4 \rightarrow CO + 2H_2$ ΔH_{298}= –44.2 kJ mol^{-1} Partial oxidation (2)

$CO_2 + CH_4 \rightarrow 2CO + 2H_2$ ΔH_{298}= 247 kJ mol^{-1} Dry reforming (3)

$2H_2O + CH_4 \rightarrow CO_2 + 4H_2$ ΔH_{298}= 169 kJ mol^{-1} Steam reforming (4)

$2CO \rightarrow CO_2 + C$ ΔH_{298}= –172 kJ mol^{-1} Boudouard reaction (5)

$CH_4 \rightarrow C + 2H_2$ ΔH_{298}= 75 kJ mol^{-1} Decomposition (6)

$CO_2 + H_2 \rightarrow CO + H_2O$ ΔH_{298}= 41 kJ mol^{-1} RWGS (7)

$CO_2 + 2H_2 \rightarrow C + 2H_2O$ ΔH_{298}= –90 kJ mol^{-1} Hydrogenation (8)

☆ In memoriam Prof. Dr. Dangsheng Su – friend and colleague.

* Corresponding author.
E-mail address: lunkenbein@fhi-berlin.mpg.de (T. Lunkenbein).

https://doi.org/10.1016/j.jechem.2020.03.013

$CO + H_2 \rightarrow C + H_2O\ \Delta H_{298} = -131$ kJ mol^{-1} Hydrogenation (9)

Important advances in the technology of DRM have been achieved over the past decades, which include the development of protocols to synthesize complex efficient catalysts [8,13,14] or the generation of insights into their working principles and into their deactivation mechanisms [9,15]. However, some aspects of the catalytic process such as the interplay between surface chemistry and activity are not entirely understood [16].

Although less active and prone to deactivation, Ni-based catalysts are preferred for industrial applications due to their low cost. The deactivation of Ni catalysts is often a consequence of carbon accumulation on the catalyst surface under reaction conditions [8,9,14,17–19]. For instance, in situ TEM imaging of the Ni catalyst has shown that tubular graphitic nanofibers can grow on metallic nanoparticles at temperatures as low as 500 °C in a H_2–CH_4 mixture [15]. This indicates that the recombination of surface carbon into volatile species can be kinetically hindered if the system is deficient in reactive surface oxygen species [18].

Using *operando* techniques, where structural and morphological properties and the activity of the catalyst are recorded simultaneously, it has been suggested that surface oxygen species play a key role in DRM (Eq. (3)) [18] and related catalytic reactions such as the partial oxidation of methane (POM, Eq. (2)) [20] as well as the methanation of CO_2 [21–23]. The main advantage of an *operando* approach is that changes which the studied systems may undergo when moving environments are avoided [16,24,25]. However, the majority of *operando* studies are based on theoretical [18], diffractometric [20], or spectroscopic [21–23] techniques. A direct visualization of surface processes for DRM using *operando* electron microscopic techniques has, to our knowledge, not been achieved to date.

Recently, the potential of environmental scanning electron microscopy (ESEM) for the study of surfaces has been unfolded [26,27]. Here, we report for the first time on the direct visualization of the surface dynamics of Ni catalysts under conditions of DRM inside the chamber of a modified environmental scanning electron microscope which was coupled to a mass spectrometer (MS). A continuous quartz tube reactor compatible with the capabilities of the ESEM was used to correlate the different surface processes of the catalyst, such as dynamics and transformations, with the catalytic conversion. These results were complemented with high resolution transmission electron microscopy (HRTEM) images and electron energy loss spectroscopy (EELS) investigations of the catalyst samples prepared for the TEM by focused ion beam (FIB). Our findings demonstrate the importance of oxide-metal phase transitions and surface transformations as key features for the catalytic reaction. As such, our study reveals an intimate link between the surface states and the rate of synthesis gas production.

2. Experimental

2.1. Sample preparation

A Ni foil (99.994% purity, 0.25 mm thick) from Alpha Aesar, and a Ni foam (95% porosity, 99.5% purity) from Goodfellow were used for the experiments. The Ni foil was used as a reference during the installation of the setup, while the foam was used for the measurement of the catalytic activity. The foil was cut into discs (diameter: 3 mm) and subjected to five consecutive acid (3% HCl) and base (3% KOH) treatments. Each treatment was performed for 5 min under sonication at room temperature (RT). Subsequently, the catalyst was rinsed with deionized water and dried. A K-type thermocouple was spot-welded on the sample surface. The Ni foam was cut into cylinders (diameter: 4 mm, length: 6 mm; weight: 35.2 mg) and placed inside the catalytic reactor. Then, the foam was oxidized for 1 h in the quartz tube reactor (Fig. 1) in synthetic air at 550 °C.

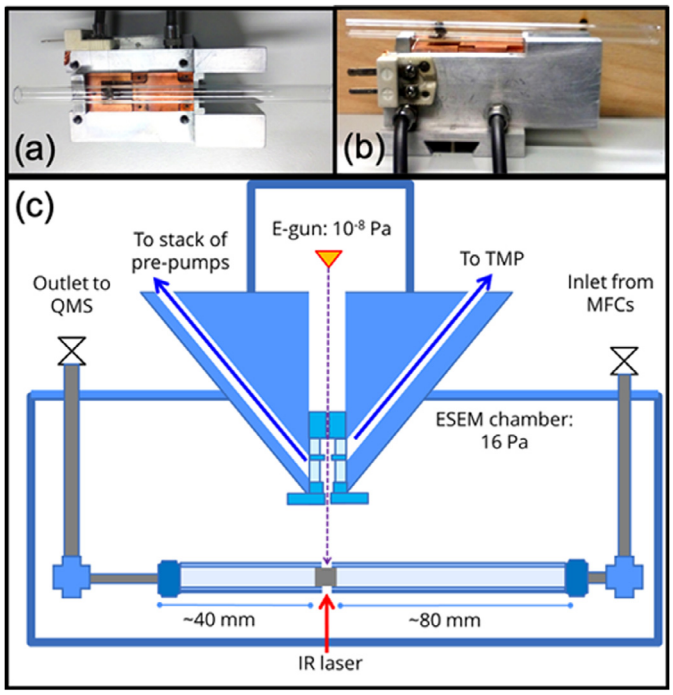

Fig. 1. The quartz tube reactor. (a) Side view and (b) top view of the laser-based heating stage, the mounted continuous quartz tube reactor and the Ni catalyst. (c) Schematics of the ESEM chamber, including the applied quartz tube reactor used for the investigation of Ni catalysts.

2.2. ESEM setup

A commercially available environmental scanning electron microscope (ESEM, FEI Quanta 200) was equipped with a homebuilt laser heating stage (Limo 40-F200-DL808-S1805, 808 nm, 40 W) and a gas feeding system [28]. Oxygen and moisture traps were installed in the gas lines (Agilent). The flow of gases was controlled by calibrated mass flow controllers (Bronkhorst). Prior to the introduction of gases into the reactor, the exhaust line of the gas feeding system was evacuated using a scroll pump to avoid any pressure overshoot. A graphical representation of the experimental setup can be found in Fig. 1. Images of the catalyst during reaction were recorded every 17.75 s with the FEI large field detector using acceleration voltages between 7.5 kV and 10 kV. The working distance was kept at 10 mm. Catalytic experiments were performed in a continuous flow quartz tube reactor located inside the ESEM chamber (Fig. 1). Using the quartz tube reactor (length: 12 cm, inner diameter: 6 mm, wall thickness: 2 mm) the sample could be kept under consistent and reproducible gas flow conditions. Surface oxidation of the sample was also reduced by the preferential direction of the gas flows towards the surrounding chamber. The outlet of the tube was connected to a quadrupole mass spectrometer (MS, Pfeiffer Prisma QMS 200). Two circular windows (diameter: 3 mm) were drilled onto the top and bottom walls of the quartz tube reactor for SEM imaging and sample heating, respectively. The catalyst was placed in the space between the circular windows. A stack of three scroll pre-pumps was used to evacuate the chamber and to ensure pressure stability. The influence of the electron beam on the reaction and surface dynamics was excluded by beam-on-beam-off studies.

2.3. Reduction of the catalyst and effect of base chamber pressure

At the start of each experiment, the ESEM chamber was evacuated for 8 h to obtain a pressure below 1.0×10^{-5} Pa to eliminate any residual oxygen and moisture. Afterwards, Ar was introduced as a carrier and internal standard for calibration (flow: 0.30 $mL_N min^{-1}$, purity: 5.0, Westfalen) and the gas composition was monitored by the MS. Ni catalysts were reduced in a H_2 (0.7 $mL_N min^{-1}$): Ar (0.3 $mL_N min^{-1}$) mixture at 900–950 °C for 120 min, with a pressure of 246 Pa inside the quartz reactor and a chamber pressure of 16 Pa. After the reduction, the H_2 flow was switched off in order to assess the surface stability of the oxophilic catalyst.

2.4. Thermal cycling experiments of synthesis gas production

The reaction mixture composed of Ar (0.3 $mL_N min^{-1}$): CO_2 (0.3 $mL_N min^{-1}$, purity: 5.0, Westfalen): CH_4 (0.4 $mL_N min^{-1}$, purity: 5.5, Westfalen) was introduced at RT [8]. Experiments were conducted in the low-vacuum mode of the microscope with a pressure of 246 Pa inside the quartz tube reactor and a chamber pressure of 16 Pa. The Ni catalyst was ramped to 770 °C in the reaction mixture ($t = 0$ min). After 20 min, the temperature was raised to 890 °C and kept for 20–30 min, then reduced to 770 °C. Thermal cycling between 770 °C and 890 °C was performed four times in order to characterize the reversibility of chemical dynamics in the regimes of low and high activities. The thermal cycling experiment was repeated using an isotope labelled $C^{18}O_2$ (100.00 vol%, Westfalen).

2.5. Temperature and time dependence of the catalytic production of synthesis gas

In the presence of the gas feed (Ar (0.3 $mL_N min^{-1}$): CO_2 (0.3 $mL_N min^{-1}$, purity: 5.0, Westfalen): CH_4 (0.4 $mL_N min^{-1}$, purity: 5.5, Westfalen) the catalyst temperature was stepwise increased from 700 °C to 900 °C (20 °C per step, dwell time: 25 min to 50 min). Subsequently, the catalyst was treated for 16 h at 885 °C. Finally, the reaction temperature was stepwise decreased from 885 °C to 845 °C (10 °C per step, dwell time: 35 min).

2.6. Processing of ESEM images

Analysis of the recorded SEM images was performed using ImageJ FIJI [29]. The stack of SEM images was binned (x2) and aligned (solid body registration). Image intensities were normalized (20×20 $pixel^2$, 2 standard deviations) [30] to eliminate fluctuations that originate from changes in the sample temperature and gas compositions. The normalization allows for the classification of the surface features by their characteristic intensities. The average intensity of the resulting stack was calculated and plotted as a time series.

2.7. High resolution transmission electron microscopy (HRTEM)

For HRTEM investigations, a TEM lamella of the spent catalyst was prepared with an FEI Helios NanoLab G3 FIB/SEM system using Ga ions with energies up to 30 keV. Before the sample was removed from the ESEM, carbon was deposited on the region of interest (ROI) to avoid surface oxidation during transfer. Subsequently, a Pt-C protective layer of 600 nm thickness was added to the ROI by electron beam induced deposition (EBID). Additional 600 nm of carbon were deposited by FIB to ensure sufficient protection during the subsequent ion milling. The lamella was thinned from both sides to <100 nm by a 30 kV Ga ion beam. In the final cleaning, low energy ion beams of 5 kV and 2 kV were applied to the sidewalls of the lamella. The prepared lamella was examined at RT with a double aberration-corrected JEOL JEM-ARM 200CF TEM operated at 200 kV with an emission current of 10.0 μA. EELS was performed using a Gatan GIF Quantum energy filter operated in dual EELS mode, which allows for a simultaneous acquisition of low and core loss regions. Point EEL spectra combined with scanning TEM (STEM) images were recorded on the top phase and on the metallic substrate at 10 nm below the interface. High-angle annular dark field (HAADF) STEM images were acquired with a semi-convergence angle of 20 mrad and collection angles of 80 mrad (inner) and 320 mrad (outer). EEL spectra were acquired with a semi-collection angle of 68 mrad. The identification of the dominant crystalline phases was performed with the CrysTBox package [31]. The reflections obtained during the Fast Fourier transform (FFT) analysis of the HRTEM images were fitted to known references.

3. Results

3.1. Stabilization of the oxophilic Ni surface

The surface of the Ni catalyst achieved a smooth appearance during the reduction in Ar and H_2 atmosphere. Selected images at the different stages of reduction can be found in the Supplementary Information (SI) in Fig. S1 and Video S1. Effects from trace amounts of oxidant impurities, i.e., oxygen and moisture, had to be excluded to ensure a reliable investigation of reaction-induced chemical dynamics of the oxophilic Ni surface. In order to avoid such surface contamination, modifications to the commercial setup had to be undertaken as it was found that the base chamber pressure that defines the partial pressure of residual oxygen and moisture had a significant, observable effect on the Ni surface (Figs. 2 and S2).

When the base chamber pressure, or more precisely, the pressure in high-vacuum mode, became too high, the reduced Ni surfaces were found to oxidize or reconstruct prior to the catalytic reaction (Fig. 2). At a base chamber pressure of ~10^{-3} Pa, for instance, the Ni surfaces were found to be covered by oxides of a bright appearance within 5 min of removing the H_2 from the gas stream (Fig. 2a and b). At base pressures of ~10^{-4} Pa, surface reconstructions could be observed in the SEM images (Fig. 2c and d). After reducing the base chamber pressure further into the 10^{-6} Pa regime by modifying the vacuum system of the microscope and placing the Ni sample in the continuous quartz tube reactor (Fig. 1), the reduced and annealed surfaces were stable in a flowing Ar atmosphere for more than 6 h (Fig. 2e and f). We attribute this to the diminished partial pressure of oxygen when the catalyst was placed inside the quartz tube reactor rather than directly into the ESEM chamber (Fig. S3).

3.2. Identification of the surface states

Significant changes in the ESEM image intensities were measured during the catalytic reaction (Fig. 3). The sample which remained after the catalytic reactions was retrieved and thinned into a TEM lamella (Fig. S4) and analyzed by HRTEM imaging (Fig. S5) and STEM-EELS measurements (Fig. S6) in order to assess the chemistry of the phases that were observed in the ESEM images. It was found that oxygen-containing and oxygen-absent phases coexisted in the sample. Theophrastite (hcp-NiO, Fig. S5a) and Bunsenite (fcc-NiO, Fig. S5b) were identified as oxidic phases that could accumulate on the catalyst surface, while the phase assignment of the substrate did not entirely match expected standard phases of Ni (fcc), Ni (hcp), Ni_3C, or NiH_x (Fig. S5a).

Based on these findings and in agreement with HRTEM results, we assigned the lower ESEM image intensities to the metallic phase and the higher ESEM image intensities to oxide is-

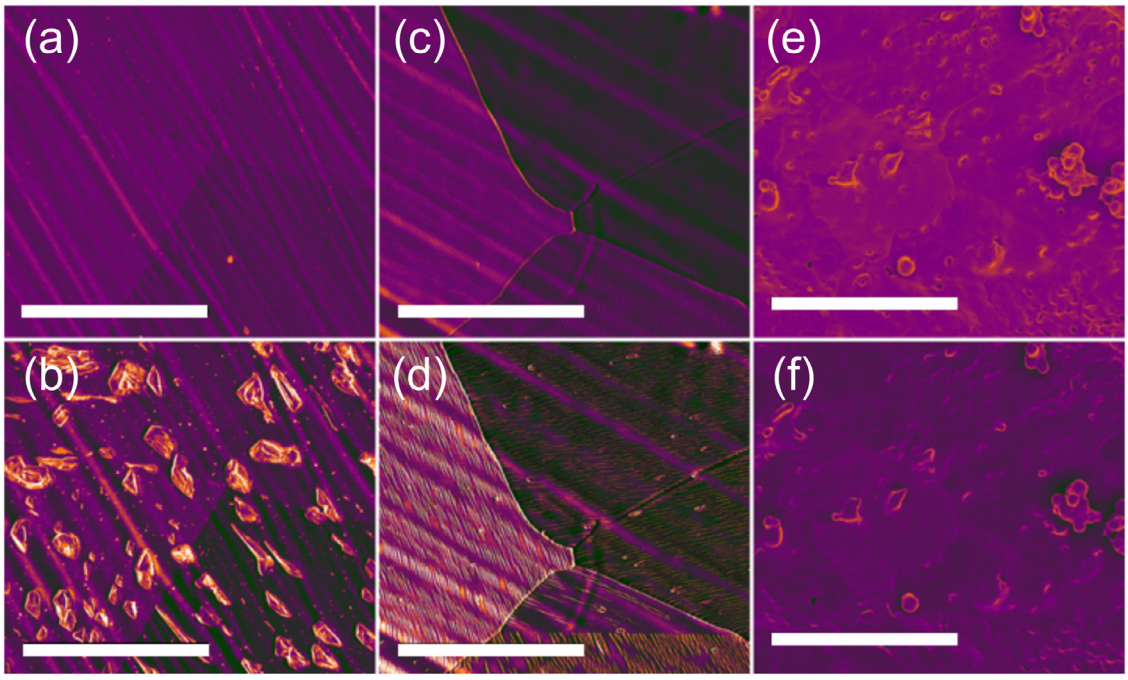

Fig. 2. The stability of the reduced Ni surface at 950 °C in a gas stream of pure Ar was found to depend on the base pressure of the chamber. (a) ESEM images of a Ni foil recorded in H_2: Ar (0.7 $mL_N min^{-1}$: 0.3 $mL_N min^{-1}$) and (b) recorded 5 min after switching off the H_2 flow at a base pressure of 10^{-3} Pa. (c) ESEM images of a Ni foil recorded in H_2: Ar (0.7 $mL_N min^{-1}$: 0.3 $mL_N min^{-1}$) and (d) recorded 5 min after switching off the H_2 flow at a base pressure of 10^{-4} Pa. (e) ESEM images of a Ni foam recorded in H_2: Ar (0.7 $mL_N min^{-1}$: 0.3 $mL_N min^{-1}$) and (f) recorded 240 min after switching off the H_2 flow at a base pressure of 10^{-6} Pa and after installation of the quartz tube reactor. Original images are presented in Fig. S2. The scale bars are 50 µm.

lands which grew on top of the metallic substrate. Throughout the manuscript, the increased image intensities were assigned to the presence of oxides, while low image intensities were assigned to a crystallographically ill-defined metallic substrate.

3.3. Catalytic production of synthesis gas during temperature cycling

A summary of the results which were obtained during the thermal cycling experiments of the Ni catalyst in the DRM mixture is depicted in Fig. 3. A movie corresponding to collated ESEM images is provided in the Supplementary Information as Video S2. No catalytic production of H_2 and only slight production of CO were detected at 770 °C (Fig. 3a) for each temperature cycle. However, during this low temperature treatment, the presence of oxides was found to increase. Synthesis gas was produced after increasing the catalyst temperature to 890 °C (Fig. 3a). The production rates for CO and H_2 were found to correlate during this stage. The formation traces showed an initial steep increase which peaked in a local maximum and decayed subsequently into a steady regime during the isothermal treatment at 890 °C. In line with this observation, the reaction traces of CH_4 and CO_2 decreased at 890 °C. However, the trends for CO_2 and CH_4 were different. While the trace for CH_4 inversely resembled the curves of H_2 and CO, the trace of CO_2 was characterized by sharp consumption peaks at the beginning of the treatment at 890 °C with an average full width at half maximum (FWHM) of 10.2 min (Fig. 3a). These CO_2 peaks subsequently reached the base value of CO_2 during the regime of high activity. The same traces also showed a slight CO_2 consumption in the low activity regime at 770 °C, indicating the formation of micrometer sized oxide islands on the surface. In addition, during the low temperature treatment at 770 °C (Fig. 3a) small amounts of H_2O were produced. Furthermore, a small peak appeared in the water traces at the beginning of the high temperature treatment (this is indicated by arrows in Fig. 3a). The production of water was found to increase after the first cycle of synthesis gas production, which was followed by a steady decay for additional temperature cycles (Figs. 3a and S8). The calculated H_2: CO ratio was found to be larger than the expected stoichiometric value for DRM (1.00, Fig. 3a, Eq. (3)). At the beginning of each treatment at 890 °C, the H_2: CO ratio (Fig. 3a) approached 3 and subsequently decayed into a steady value of 1.92.

The depletion of surface oxide islands as detected by the decreasing image intensities was realized at 890 °C. Cycling the temperature within the chosen temperature regimes reversed the catalytic activity as well as the image intensities, i.e. the presence and absence of oxides had an intimate link with the production of synthesis gas. In brief, the flat and smooth Ni surface which pointed to the presence of an ill-defined metallic state was prevalent during the production of synthesis gas. In contrast, rough and bright surfaces which indicated the presence of surface oxide islands were observed during the stage of low activity.

The rate of change of the image intensities and reaction traces (from Fig. 3a) were computed from their 1st derivatives with respect to time (Fig. 3b). The negative peaks in the 1st derivative of the image intensity (Fig. 3b) indicated a fast depletion of the oxide phases which occurred when the catalyst was heated from 770 °C to 890 °C. These negative peaks in the image intensities were accompanied by positive peaks in the 1st derivatives of the production rates of H_2 and CO and negative peaks in the 1st derivatives of the reactants CH_4 and CO_2. During cooling, negative peaks arose in the 1st derivatives of the production rates of H_2 and CO which were accompanied by positive peaks in the analogues of CH_4 and image intensities. This observation highlights that a fast surface oxidation paralleled the deactivation of the catalyst during cooling. The positive peaks in the 1st derivatives of the CO_2 traces were absent during cooling (Fig. 3b), which pointed to a steady CO_2 consumption. Moreover, the trace of H_2O had a complex be-

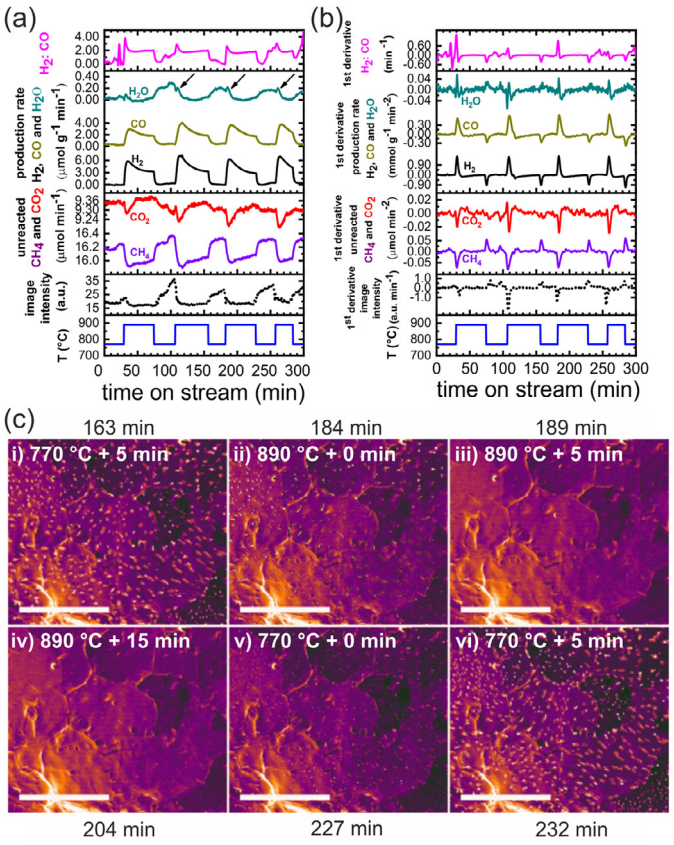

Fig. 3. Compilation of catalytic and surface observables of synthesis gas production over metallic Ni foam during thermal cycling between 770 °C and 890 °C. (a) From bottom to top: time series of simultaneously recorded temperature of the catalyst, image intensities and reaction traces of CH_4, CO_2, O_2, H_2, CO, H_2O, and the H_2: CO ratios. (b) First derivative of time of the observables depicted in (a). (c) ESEM images recorded under reaction conditions at selected times of the 3rd thermal cycle. Time on stream: 158 to 240 min. Gas mixture: 0.3 $mL_N min^{-1}$ Ar; 0.3 $mL_N min^{-1}$ CO_2; $mL_N min^{-1}$ CH_4. Original grayscale images can be found in Fig. S7. The scale bars are 50 µm.

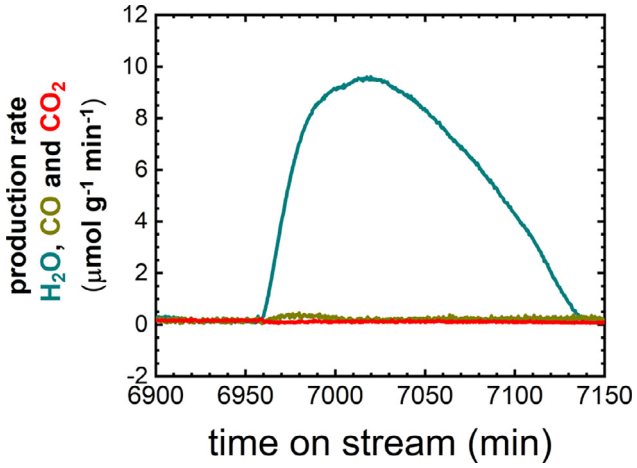

Fig. 4. Traces of volatile oxidation products generated during the treatment of the spent Ni catalyst in an oxidizing atmosphere. Gas mixture: 0.6 $mL_N min^{-1}$ Ar; 0.4 $mL_N min^{-1}$ O_2. Isothermal treatment at 930 °C for 210 min. Start of heating: 6959 min.

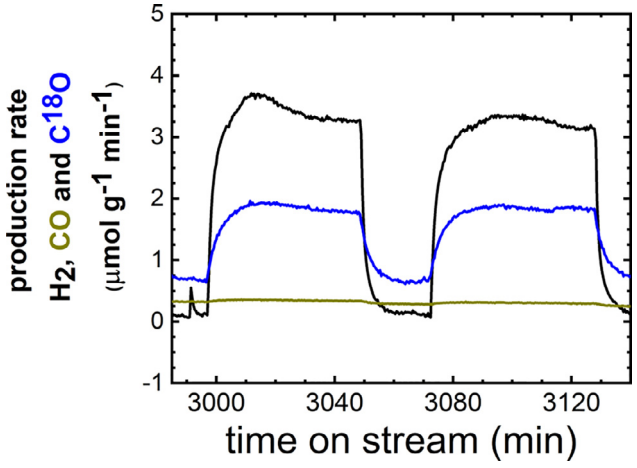

Fig. 5. Synthesis gas production over the Ni catalyst during thermal cycling between 770 °C and 890 °C with $C^{18}O_2$. Gas mixture: 0.3 $mL_N min^{-1}$ Ar; 0.3 $mL_N min^{-1}$ $C^{18}O_2$; 0.4 $mL_N min^{-1}$ CH_4.

havior featured by a small and broad positive peak at the beginning of the treatment at 770 °C indicating the formation of water. At the beginning of the treatment at 890 °C a sharp positive peak arose which was immediately followed by a negative peak. This implies that an additional production of H_2O was initialized within a small temperature increment which was followed by a fast expenditure. The combined information depicted in Fig. 3(a and b) indicate that the most significant changes in the production rates of CO and H_2 inversely correlated with the fast variations of the image intensities, which suggests a strong correlation between the surface coverage by oxide islands and the catalytic performance.

Selected ESEM images of the Ni surface acquired during the 3rd temperature cycle (time on stream: 158 to 260 min) are shown in Fig. 3(c). The images show the presence of oxide islands (regions of high image intensity) after 5 min of exposure of the catalyst to the DRM mixture at 770 °C (Fig. 3c–i). The depletion of these oxide islands was initiated with the temperature increase to 890 °C. The oxides were consumed after 5 min of isothermal treatment at 890 °C (Fig. 3c-ii and c-iii) and the surface reached a smooth appearance (Fig. 3c-iv). Furthermore, it was found that the oxide islands grew at close to identical locations during each cycle (Fig. 3c-v and c-vi, Video S2). The reversible occurrence of the oxides during temperature cycling suggests that the observed phase transition can act as an internal switch between the active and inactive states.

The nature of the Ni substrate was further assessed after the reaction in the quartz tube reactor by thermal treatment in an oxygen-containing atmosphere at 930 °C for over 180 min. The corresponding MS data (Fig. 4) show the formation of H_2O and trace amounts of CO and CO_2. The integrated production rate for H_2O was 45.2 µmol, which corresponded to 90.4 µmol of remaining H in the catalyst after the production of synthesis gas. In contrast, only 0.89 µmol of C-containing compounds were produced. This suggests the presence of dissolved hydrogen species or of substoichiometric NiH_x phases and a comparatively small accumulation of carbon after the catalytic process.

In order to identify the source of oxygen and to exclude the presence of trace amounts of oxidants in the chamber as a potential source, the temperature cycling experiment was repeated using isotope-labelled $C^{18}O_2$. The vast majority of CO produced during the experiment was found to be ^{18}O labelled (Fig. 5). This indicates that CO_2 was the main oxygen source not only for CO, but also for the formation of the oxides which were observed on the catalyst surface. In addition, the H_2: $C^{18}O$ ratio was found to be larger than 1.00.

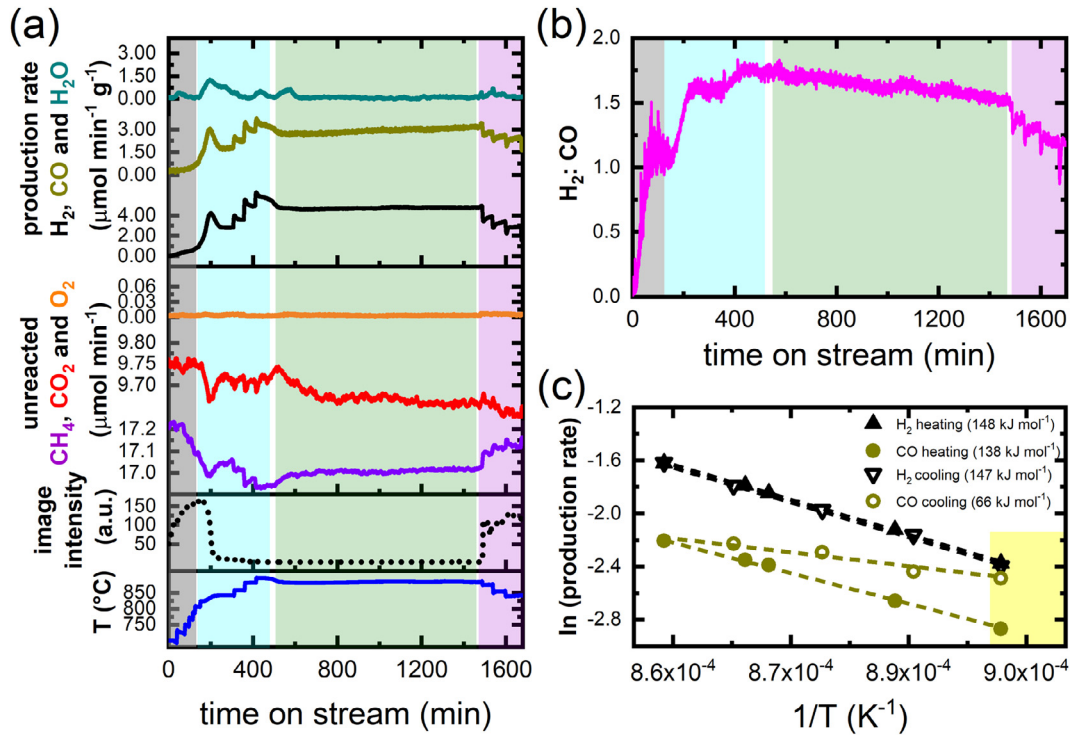

Fig. 6. Compilation of catalytic and surface observables during synthesis gas production over metallic Ni catalyst in the temperature range between 700 °C and 900 °C. (a) From bottom to top: time series of simultaneously recorded temperature of the catalyst, image intensities, and reaction traces of CH_4, CO_2, O_2, H_2, CO and H_2O. Color coded areas correspond to consecutive stages of the experiment. (b) Time series of the measured H_2: CO ratio. (c) Arrhenius plots of the catalytic production of H_2 and CO. The color region in (c) marks the temperature range at which oxides were observed. Gas mixture: 0.3 $mL_N min^{-1}$ Ar; 0.3 $mL_N min^{-1}$ CO_2; 0.4 $mL_N min^{-1}$ CH_4. Reaction onset: 806 °C. Oxidation onset during cooling: 846 °C.

3.4. Temperature and time dependence of the catalytic production of synthesis gas

The time-resolved observables of the catalytic system at different temperatures and under isothermal conditions at 885 °C are shown in Fig. 6. In this experiment, the temperature was stepwise increased and decreased in the interval between 700 °C and 900 °C. Fig. 6 was divided into four consecutive regions (color-code): (i) The gray region corresponds to the heating of the catalyst from 700 °C to 806 °C, at which no catalytic production of synthesis gas was observed. (ii) The blue highlighted region denotes the temperature interval between 806 °C and 890 °C subsequent to the catalytic activation. (iii) The green region depicts the isothermal treatment at 885 °C for 16 h, and (iv) the pink region shows the information on the catalytic performance during cooling from 885 °C to 846 °C.

The data in Fig. 6(a) demonstrates that the catalyst was inactive in the production of synthesis gas at temperatures between 700 °C and 806 °C (Fig. 6a, gray area). Simultaneously, the intensity of the in situ collected ESEM images continuously increased (Fig. 6a). The catalytic production of H_2 and CO initiated at 806 °C (Fig. 6a, blue area), while the image intensities decreased abruptly during the catalytic activation. Further increasing the reaction temperature to 890 °C led to enhanced production of synthesis gas. For each temperature step, the formation rates of H_2 and CO peaked in local maxima which were followed by partial deactivation and subsequently levelled off into steady values. The traces corresponding to the production of CH_4 showed the opposite trends, while for CO_2 the traces decreased during the initiation of each temperature step, which reached a local minimum and subsequently increased during the deactivation of the reaction. Simultaneously, the image intensities steadily decreased and reached a global minimum value. During the isothermal treatment at 885 °C for 16 h (Fig. 6a, green region) the catalyst showed its highest activity. While the production rate of H_2 remained steady, a slight increase was observed in the production rate of CO. In line, the traces of CH_4 reached steady values, while the traces of CO_2 decreased simultaneously.

A stepwise decrease in the reaction temperature (Fig. 6a, pink region) was applied after the isothermal treatment of 16 h in order to study the reversibility of the phase transitions. During this treatment, the production rate of synthesis gas decreasd. The production rates of H_2 and CO exhibited reversed trends compared to their respective behaviors during heating. Furthermore, the image intensities began to increase. The trace of O_2 maintained a steady value close to zero during the experiment, while a small production of H_2O was detected only during the early stages of the activation of the reaction (Fig. 6a). The same trace exhibited slight fluctuations around the base values during the most of the experiment.

H_2: CO ratios are presented in Fig. 6(b). During activation the measured H_2: CO ratio fluctuated between 1.5 and 1.8 (Fig. 6b, blue region), which is in line with the observation that other reaction mechanisms aside from DRM could simultaneously participate in the catalytic turnover. The H_2: CO ratio decreased continuously during the isothermal treatment at 885 °C (Fig. 6b, green region) and approached 1.00 during cooling to 846 °C. Thus, the reaction progressively evolved towards product ratios which were characteristic for DRM.

The Arrhenius plots presented in Fig. 6(c) clearly show that the production of H_2 was reversible with temperature variations, while the curves for CO followed different routes during heating and cooling. The estimated activation energies (E_{app}) for the production of H_2 were 148 kJ mol^{-1} independently of the catalyst history. For the production of CO it was found that E_{app} was 138 kJ mol^{-1} dur-

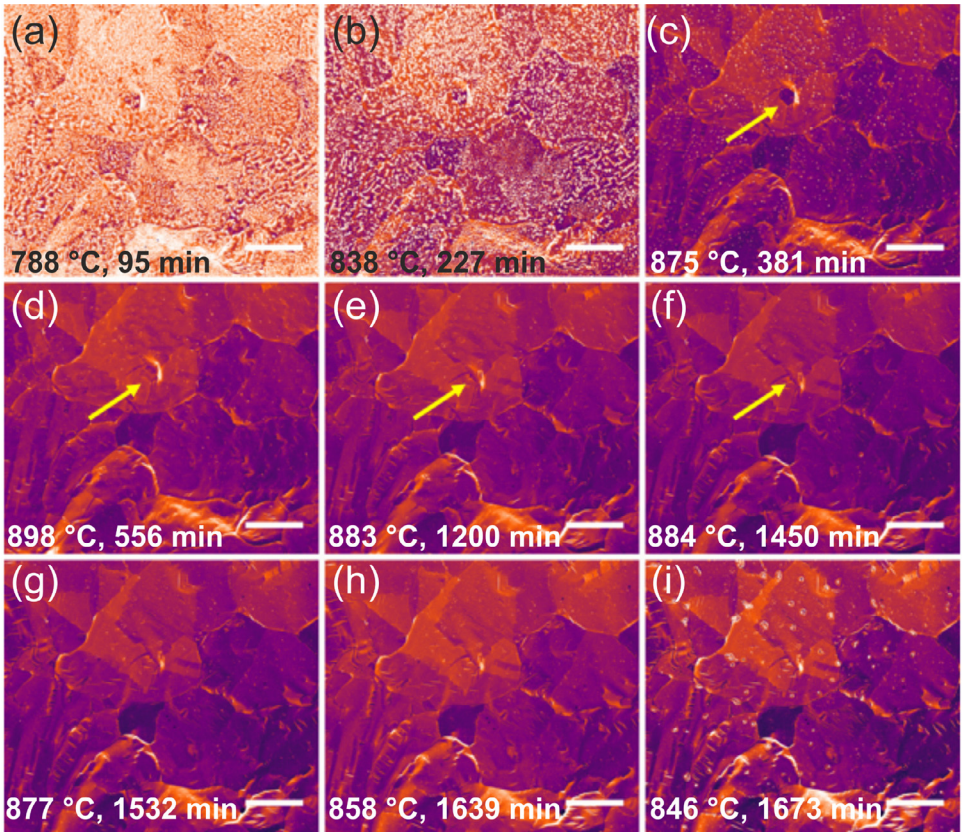

Fig. 7. Selected ESEM images acquired during the catalytic production of synthesis gas at different temperatures and times on stream. (a–c): ESEM images that were recorded during stepwise heating of the Ni foam at different temperatures; (d–f): ESEM images that were recorded during isothermal treatment at 885 °C for 16 h; (g–i): ESEM images that were recorded during cooling from 885 °C to 846 °C. Arrows in (c—f) display grain growth. Gas mixture: 0.3 $mL_N min^{-1}$ Ar; 0.3 $mL_N min^{-1}$ CO_2; 0.4 $mL_N min^{-1}$ CH_4. Original grayscale images can be found in Fig. S9. The scale bars are 20 µm.

ing heating and 66 kJ mol^{-1} during cooling. This result suggests that the dominant pathway of CO production shifted over time. The colored area at the high 1/*T* border of Fig. 6(c) corresponds to the temperature range at which oxidic phases were present on the catalyst surface.

The surface characteristics during temperature treatment were monitored online by ESEM imaging (Fig. 7). A movie composed of collated ESEM images is provided in Video S3. In the non-active temperature regime below 806 °C, the surface appeared populated with bright spots (Fig. 7a). After activation and subsequent temperature increase the bright spots that are characteristic for oxides were progressively depleted from the surface (Fig. 7b–d, Video S3). At temperatures above 875 °C the metallic substrate composed of µm-sized domains became the dominant surface state (Fig. 7d–f), which remained stable under the applied working conditions. Few changes of the catalyst surface were observed during this stage (See feature indicated by an arrow from Fig. 7c–f, Video S3) which can be best described as metallic grain growth. During cooling, the image intensities increased (Fig. 7f–h) and oxide islands started to form on the surface of the catalyst at 846 °C (Fig. 7i, Video S3). These island-like regular-shaped oxide phases (Fig. 7i) differed morphologically from the pristine oxides that were observed at the beginning of the experiment (Fig. 7a). In addition, the surface of the metallic substrate started to transform (Fig. 7, Video S3). This suggests that the catalyst underwent irreversible morphological transformations during the long-term treatment.

In summary, the Ni catalyst had an oxidized surface at temperatures below 806 °C, and a progressively reduced surface above the temperature of initiation. The catalyst surface reoxidized after cooling to 846 °C.

4. Discussion

A first but crucial step for realizing successful *operando* studies of an oxophilic catalyst is to avoid the presence of any oxidizing impurities that can alter the active surface. Air leaks in the setup can cause misleading dynamics of the catalyst and misinterpretations of observed phenomena. The minimization of air leaks and the installation of the quartz tube reactor (Fig. 1) were crucial as the formation of oxides and surface reconstructions related to oxygen adsorption [32,33] were efficiently suppressed (Fig. 2). The setup presented here provided for a contamination-free study, since the reduced catalyst surface remained stable for more than 6 h (Fig. 2) in an atmosphere of flowing argon.

The results from the present study are summarized in Scheme 1. In line with previous studies [20,34], our combined microscopy and catalytic results (Figs. 3, 6 and 7) show that the reduced Ni surface progressively becomes the dominant state during the catalytic production of synthesis gas.

DRM on supported catalysts appears to follow a stepwise bi-functional mechanism, where CH_4 is activated on the metal and CO_2 on the support [22]. In the absence of a support, the reactants have to be activated on the metal and compete for the adsorption sites. The observed production trends of synthesis gas show the bi-functional nature of the Ni surface which can simultaneously activate CO_2 and CH_4 in the absence of a support. In agreement with earlier studies [18,23], the dissociative activation of CO_2 already takes place at temperatures below the onset temperature of the catalytic production of synthesis gas, as can be seen by the formation of surface oxide islands and slight production of CO at 770 °C (Figs. 3, 6, 7, S5 and S6, Video S2 and Video S3). The high tem-

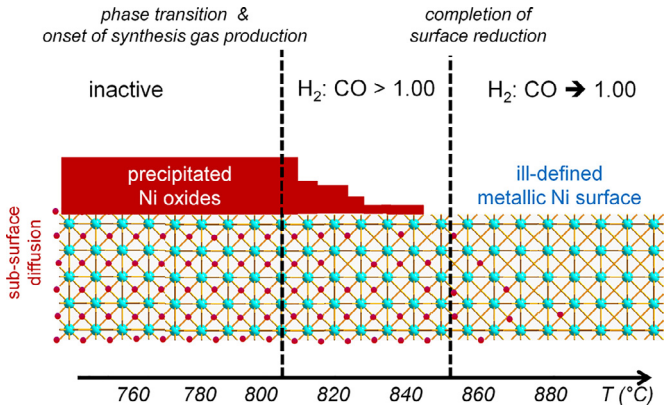

Scheme 1. Schematic representation of the oxide-metal phase transition that controls the catalytic behavior during the production of synthesis gas over Ni catalysts. In the temperature regime at which the reaction had not started yet, the surface was found to be oxidized. The oxide-metal phase transition occurred simultaneously to the initiation of synthesis gas production with product ratios higher than 1.00. The product ratios approached 1.00 after extensive treatment.

perature required to initiate the production of synthesis gas can be attributed to the activation of CH_4 [35]. Surface species which originate from the dissociation of methane are oxidized by the metal oxides formed by CO_2 to generate CO and H_2O (Fig. 3) [36]. H_2 is then formed via recombination of atomic H species. More reduced surface sites are made available for CH_4 activation through the initial depletion of oxides from the catalyst. Once the reduction is triggered, the surface stays in the reduced state. Thus, the catalyst surface adapts to the applied chemical potential.

While the phase transitions seem to be reversible for short temperature cycling (Fig. 3), the observed changes on the surface during the long-term experiments (Fig. 7, Video S3) and the formation of different shaped oxides after cooling suggest the occurrence of irreversible surface transformations. Reversible phase transitions, i.e. structural dynamics, and irreversible morphological transformations are part of chemical dynamics [37]. Their visualization and the discovery of their effect on the catalytic performance have been recently accomplished [38]. This interpretation is also in line with the results observed by near-ambient-pressure XPS of metallic Ni during the catalytic oxidation of methane [34] and propane [16].

During activation, the reaction mechanism drastically favored H_2 formation over CO as indicated by the relatively large initial H_2: CO ratio (Figs. 3 and 6) which was found to decrease over time. This indicates that the catalytic surface is in a non-equilibrated state under these conditions (see change of image intensities in Figs. 3a, c and 7). Catalytically and thermally induced side reactions may dominate at this point. This could prompt the occurrence of consecutive reactions over complex pathways to form H_2, CO, H_2O and CO_2. A likely scenario could involve steam reforming of methane at which the H_2: CO ratio equals 3.00 (Eq. (1)). As has been shown in Fig. 3 water is formed in the non-active regime at 770 °C. The increase in the water production rate after the first temperature cycle and the steady decrease in the water signal for consecutive cycles (Fig. S8) at constant gas flow may indicate that the storage of hydrogen which is produced during the active regime is irreversible for different cycles and that this hydrogen can act as a source for water formation at lower temperatures [39]. In addition, water can be formed during the depletion of the oxides at the early stages of the reaction (see arrows in Fig. 3a).

Furthermore, while the consumption of CO_2 in the state of low activity can be understood as the formation of micrometer-sized oxide islands which are visible in the ESEM images (Figs. 3 and 7), the interpretation of the unusual behavior of the CO_2 traces during the reaction (Figs. 3 and 6) is not trivial. The initial high CO_2 uptake could be further interpreted as the thermally induced filling of defective surface and sub-surface states that may act as oxygen reservoirs for the reaction. As water can be excluded as a contaminant (Fig. 2) these reactive oxygen species could form water in situ with nascent hydrogen located at the (sub-) surface which can then result in steam reforming-like initial H_2: CO ratios (Eq. (1), Figs. 3 and 7).

Alternatively, the initial high H_2: CO ratio may be explained by a pseudo POM (Eq. (2)) mechanism at which CO formation is inhibited by the presence of a large amount of oxides. The absence of CO_2 consumption at 890 °C (time on stream higher than 5 min, Fig. 3a) could suggest that CO_2 adsorption is inhibited by the presence of stored and activated oxygen. The reaction proceeds preferentially with these species instead of CO_2. At steady state during the first 30 min of reaction the H_2: CO ratio approaches values representative for the POM reaction (Eq. (2)) where methane reacts not with CO_2, but with activated oxygen species. The H_2: CO ratio approached values more representative of DRM only after several hours of isothermal treatment at high temperatures (Fig. 6). This suggests the presence of sub-surface oxygen which is slowly consumed during the long-term experiments. The reaction evolved towards DRM and was accompanied by slight activation of the formation of CO and a decreasing trace of CO_2 (Fig. 6). The cause could be a gradual change of the dominant path of CO formation (Fig. 6c) when oxygenate species which are stored in the catalyst are extensively depleted.

The fastest increase in production rates was shown to occur during the oxide depletion, i.e. during the reaction induced oxide-metal phase transition (Fig. 3) which led to the exposure of a large amount of metallic surface sites to the reactive environment. This transition of the oxide phases also caused changes in the H_2: CO ratio (Figs. 3 and 6). Thermal decomposition of the oxide would have left the H_2: CO ratio unaffected. Thus, the surface species which participate in the phase transition are transferred into the gas products and partake in the observed product ratio. Note, the presented results and the provided discussion are representative for a restricted set of conditions and may look different for other (supported) catalytic systems, space velocities, time scales, temperature protocols and gas ratios.

There have been contradictory findings in the literature around the catalytic role of the in situ formed species and the presence of oxygen in the system. On the one hand, oxide phases are thought to be detrimental for the reaction as they can compete with CH_4 for metallic surface sites [40]. On the other hand, oxides are thought to maintain the catalytic activity by consuming adsorbed carbon species [18,40,41]. Their involvement during the reaction would be beneficial for the long-term stability of the catalyst, since surface carbonization and the deposition of carbon can be mitigated. The formation of carbon deposits is known to be a major cause for deactivation of reforming catalysts [2,8–10,14,15,17,19,41]. However, oxide shells that form during reductive activation to surround the supported Ni particles can suppress carbon formation while preserving a high catalytic activity [9]. It should be noted that in this study carbon accumulation was not detected. If present, even monolayers of carbon would have been detected by ESEM imaging [27]. In addition, the subsequent oxidation treatment inside the quartz tube reactor indicated that coke was not produced (Fig. 4). This experiment revealed a Ni:H ratio in the spent catalyst of 6.6, which suggests the presence of dissolved hydrogen species or the formation of sub-stoichiometric hydrides in the sub-surface or in the bulk which may be responsible for the water formation at low temperature. For comparison, the Ni: C ratio was 671.

5. Conclusions

We have presented an ESEM investigation of oxophilic Ni surfaces during the production of synthesis gas from DRM mixtures. Modifying a commercially available ESEM enabled us to directly visualize the catalyst under working conditions. In particular, the use of a continuous quartz tube reactor facilitated the detection and quantification of the catalytic conversion. The study further highlights the importance of contamination-free sample environments in order to convert visual and catalytic observables into reliable knowledge of the working principles of the catalytic system.

Temperature cycling combined with online mass spectrometry and real-time imaging revealed the presence of chemical dynamics in the form of oxide-metal phase transitions that were found to initiate the catalytic production of synthesis gas, and morphological transformation that caused irreversible surface changes. Our results showed that stoichiometries other than DRM were dominant at early stages of the catalytic activation. The catalytic observables evolved towards values representative of DRM only after several hours of treatment at high temperature due to a possible shift in the mechanism of formation of CO. These observations can be explained by the presence of a (sub-) surface reservoir of active species which deplete during the reaction.

Further studies need to be conducted to conclude on the influence of space velocity and gas ratio on the reaction mechanism, surface and bulk chemistry, and stoichiometry of the involved oxide phases. Nevertheless, our work highlights the importance of *operando* approaches to investigate simultaneously several aspects of the reaction system, including the mechanisms of activation and deactivation of heterogeneous catalysts. Overall, it was shown that the catalytic production of synthesis gas was activated by the presence of oxide-metal phase transitions. These marked a clear distinction between active and inactive states.

Declaration of Competing Interest

The authors declare that they have no known competing financial interests or personal relationships that could have appeared to influence the work reported in this paper.

Acknowledgments

We acknowledge Dr. Marc G. Willinger and Dr. Zhu-Jun Wang for the construction of the initial ESEM setup and of the heating stage during their stay at FHI. We are further grateful to Dr. Cédric Barroo and Dr. Andrey Tarasov for fruitful discussions. The authors thank the mechanical workshop of FHI for the construction of the quartz tube reactor.

Supplementary materials

Supplementary material associated with this article can be found, in the online version, at doi:10.1016/j.jechem.2020.03.013.

References

[1] F. Fischer, H. Tropsch, Brennstoff-Chem. 9 (1928) 21–24.
[2] H. Holm-Larsen, Studies in Surface Science Catalysis Book Series 136 (2001) 441–446.
[3] L. Shi, G. Yang, K. Tao, Y. Yoneyama, Y. Tan, N. Tsubaki, Acc. Chem. Res. 46 (8) (2013) 1838–1847.
[4] J. Kehres, J.G. Jakobsen, J.W. Andreasen, J.B. Wagner, H. Liu, A. Molenbroek, J. Sehested, I. Chorkendorff, T. Vegge, J. Phys. Chem. C 116 (40) (2012) 21407–21415.
[5] M.G. Heidlage, E.A. Kezar, K.C. Snow, P.H. Pfromm, Ind. Eng. Chem. Res. 56 (47) (2017) 14014–14024.
[6] R. Schlögl, Top. Catal. 59 (8) (2016) 772–786.
[7] R. Schlögl, ChemSusChem 3 (2) (2010) 209–222.
[8] K. Mette, S. Kühl, H. Düdder, K. Kähler, A. Tarasov, M. Muhler, M. Behrens, ChemCatChem 6 (1) (2014) 100–104.
[9] K. Mette, S. Kühl, A. Tarasov, M.G. Willinger, J. Kröhnert, S. Wrabetz, A. Trunschke, M. Scherzer, F. Girgsdies, H. Düdder, K. Kähler, K.F. Ortega, M. Muhler, R. Schlögl, M. Behrens, T. Lunkenbein, ACS Catal. 6 (10) (2016) 7238–7248.
[10] J.R. Rostrup-Nielsen, J.H.B. Hansen, J. Catal. 144 (1) (1993) 38–49.
[11] R.K. Singha, A. Yadav, A. Shukla, M. Kumar, R. Bal, Catal. Commun. 92 (2017) 19–22.
[12] V. Sadykov, V. Rogov, E. Ermakova, D. Arendarsky, N. Mezentseva, G. Alikina, N. Sazonova, A. Bobin, S. Pavlova, Y. Schuurman, C. Mirodatos, Thermochim. Acta 567 (2013) 27–34.
[13] K.P. de Jong, Synthesis of Solid Catalysts, Wiley-VCH, Weinheim, 2009, pp. 33–199.
[14] M. Akri, S. Zhao, X. Li, K. Zang, A.F. Lee, M.A. Isaacs, W. Xi, Y. Gangarajula, J. Luo, Y. Ren, Y.-T. Cui, L. Li, Y. Su, X. Pan, W. Wen, Y. Pan, K. Wilson, L. Li, B. Qiao, H. Ishii, Y.-F. Liao, A. Wang, X. Wang, T. Zhang, Nat. Commun. 10 (1) (2019) 5181.
[15] S. Helveg, C. López-Cartes, J. Sehested, P.L. Hansen, B.S. Clausen, J.R. Rostrup-Nielsen, F. Abild-Pedersen, J.K. Nørskov, Nature 427 (2004) 426.
[16] V.V. Kaichev, D. Teschner, A.A. Saraev, S.S. Kosolobov, A.Y. Gladky, I.P. Prosvirin, N.A. Rudina, A.B. Ayupov, R. Blume, M. Hävecker, A. Knop-Gericke, R. Schlögl, A.V. Latyshev, V.I. Bukhtiyarov, J. Catal. 334 (2016) 23–33.
[17] H. Düdder, K. Kähler, B. Krause, K. Mette, S. Kühl, M. Behrens, V. Scherer, M. Muhler, Catal. Sci. Technol. 4 (9) (2014) 3317–3328.
[18] K. Yuan, J.-Q. Zhong, X. Zhou, L. Xu, S.L. Bergman, K. Wu, G.Q. Xu, S.L. Bernasek, H.X. Li, W. Chen, ACS Catal. 6 (7) (2016) 4330–4339.
[19] Y. Chai, Y. Fu, H. Feng, W. Kong, C. Yuan, B. Pan, J. Zhang, Y. Sun, ChemCatChem 10 (9) (2018) 2078–2086.
[20] A.A. Saraev, Z.S. Vinokurov, V.V. Kaichev, A.N. Shmakov, V.I. Bukhtiyarov, Catal. Sci. Technol. 7 (8) (2017) 1646–1649.
[21] Y. Ren, K. Yuan, X. Zhou, H. Sun, K. Wu, S.L. Bernasek, W. Chen, G.Q. Xu, Chem. A Europ. J. 24 (60) (2018) 16097–16103.
[22] P.A.U. Aldana, F. Ocampo, K. Kobl, B. Louis, F. Thibault-Starzyk, M. Daturi, P. Bazin, S. Thomas, A.C. Roger, Catal. Today 215 (2013) 201–207.
[23] B. Mutz, H.W.P. Carvalho, S. Mangold, W. Kleist, J.-D. Grunwaldt, J. Catal. 327 (2015) 48–53.
[24] G. Ertl, Angew. Chem. 120 (19) (2008) 3578–3590.
[25] S. Böcklein, S. Günther, J. Wintterlin, Angew. Chem. 125 (21) (2013) 5628–5631.
[26] C. Barroo, Z.-J. Wang, R. Schlögl, M.-G. Willinger, Nat. Catal. 3 (1) (2020) 30–39.
[27] Z.-J. Wang, J. Dong, Y. Cui, G. Eres, O. Timpe, Q. Fu, F. Ding, R. Schlögl, M.-G. Willinger, Nat. Commun. 7 (2016) 13256.
[28] Z.-J. Wang, In Situ Scanning Electron Microscopy Studies on the Dynamics of Metal-Catalyzed CVD Growth of Graphene Doctoral Thesis, Technische Universität Berlin, Berlin, 2017.
[29] J. Schindelin, I. Arganda-Carreras, E. Frise, V. Kaynig, M. Longair, T. Pietzsch, S. Preibisch, C. Rueden, S. Saalfeld, B. Schmid, J.-Y. Tinevez, D.J. White, V. Hartenstein, K. Eliceiri, P. Tomancak, A. Cardona, Nat. Methods 9 (2012) 676.
[30] A.D. Fleming, S. Philip, K.A. Goatman, J.A. Olson, P.F. Sharp, IEEE Trans. Med. Imaging 25 (9) (2006) 1223–1232.
[31] M. Klinger, A. Jager, J. Appl. Crystallogr. 48 (6) (2015) 2012–2018.
[32] G.J. Millar, M.L. Nelson, P.J.R. Uwins, J. Catal. 169 (1) (1997) 143–156.
[33] G. Somorjai, Introduction to Surface Chemistry and Catalysis, Surface Science and Catalysis, John Wiley & Sons, Inc., New York, 1994, pp. 36–75.
[34] A.A. Saraev, Z.S. Vinokurov, A.N. Shmakov, V.V. Kaichev, V.I. Bukhtiyarov, Kinet. Catal. 59 (6) (2018) 810–819.
[35] J. Wei, E. Iglesia, J. Catal. 224 (2) (2004) 370–383.
[36] A.A. Saraev, S.S. Kosolobov, V.V. Kaichev, V.I. Bukhtiyarov, Kinet. Catal. 56 (5) (2015) 598–604.
[37] R. Schlögl, Angew. Chem. Int. Ed. 54 (11) (2015) 3465–3520.
[38] M. Plodinec, H.C. Nerl, F. Girgsdies, R. Schlögl, T. Lunkenbein, ACS Catal. 10 (2020) 3183–3193.
[39] K. Delgado, L. Maier, S. Tischer, A. Zellner, H. Stotz, O. Deutschmann, Catalysts 5 (2) (2015) 871–904.
[40] S. Kawi, Y. Kathiraser, J. Ni, U. Oemar, Z. Li, E.T. Saw, ChemSusChem 8 (21) (2015) 3556–3575.
[41] J.M. Ginsburg, J. Piña, T. El Solh, H.I. de Lasa, Ind. Eng. Chem. Res. 44 (14) (2005) 4846–4854.